Available online at www.sciencedirect.com
SCIENCE DIRECT®
Computers & Fluids 35 (2006) 898–909
computers & fluids
www.elsevier.com/locate/compfluid

An evaluation of lattice Boltzmann schemes for porous medium flow simulation

Chongxun Pan [a,*], Li-Shi Luo [b], Cass T. Miller [a]

[a] *Center for the Integrated Study of the Environment, Department of Environmental Sciences and Engineering, University of North Carolina, Chapel Hill, NC 27599-7431, USA*
[b] *Department of Mathematics and Statistics, Old Dominion University, Norfolk, VA 23529, USA*

Received 29 July 2004; accepted 8 March 2005
Available online 10 January 2006

Abstract

We quantitatively evaluate the capability and accuracy of the lattice Boltzmann equation (LBE) for modeling flow through porous media. In particular, we conduct a comparative study of the LBE models with the multiple-relaxation-time (MRT) and the Bhatnagar–Gross–Krook (BGK) single-relaxation-time (SRT) collision operators. We also investigate several fluid–solid boundary conditions including: (1) the standard bounce-back (SBB) scheme, (2) the linearly interpolated bounce-back (LIBB) scheme, (3) the quadratically interpolated bounce-back (QIBB) scheme, and (4) the multi-reflection (MR) scheme. Three-dimensional flow through two porous media—a body-centered cubic (BCC) array of spheres and a random-sized sphere-pack—are examined in this study. For flow past a BCC array of spheres, we validate the linear LBE model by comparing its results with the nonlinear LBE model. We investigate systematically the viscosity-dependence of the computed permeability, the discretization error, and effects due to the choice of relaxation parameters with the MRT and BGK schemes. Our results show unequivocally that the MRT–LBE model is superior to the BGK–LBE model, and interpolation significantly improves the accuracy of the fluid–solid boundary conditions.

1. Introduction

Historically, the lattice Boltzmann equation (LBE) for modeling hydrodynamics [1,2] originated from the lattice-gas cellular automata (LGCA) [3,4]. Recently, it was shown that the LBE can be *directly* derived by discretizing the Boltzmann equation [5,6]. This not only sets the LBE method on the solid foundation of kinetic theory, but also makes the LBE method more amenable to numerical analysis. The LBE method has been shown to be equivalent to an explicit, first-order in time, second-order in space finite difference approximation of the *incompressible* Navier–Stokes equations [7–9]. Thus, the LBE method can be viewed as a discrete approximation of the incompressible Navier–Stokes equations, based on kinetic theory rather than continuum theory [10].

Due to its kinetic origin, the LBE method has some features that are significantly different from conventional computational fluid dynamics methods based on a direct discretization of the Navier–Stokes equations. Appealing features of the LBE method include programming simplicity, intrinsic parallelism, and straightforward resolution of complex solid boundaries and multiple fluid species. Hence, the LBE method has gained popularity in recent years for simulating single-fluid and multiple-fluid phase flow through porous media (cf. [11,12] and references therein). However, computational limitations remain of concern for such applications.

The most popular LBE model used in porous medium simulations is the lattice Bhatnagar–Gross–Krook (LBGK) model [13,14] with a standard bounce-back (SBB) scheme for fluid–solid boundaries. However, two common problems are encountered with this popular

* Corresponding author.
E-mail addresses: dpan@unc.edu (C. Pan), lluo@odu.edu (L.-S. Luo), casey_miller@unc.edu (C.T. Miller).

0045-7930/$ - see front matter © 2005 Elsevier Ltd. All rights reserved.
doi:10.1016/j.compfluid.2005.03.008

method. First, the LBGK model, in which the collision operator is approximated by a single-relaxation-time (SRT) approximation, has some defects such as numerical instability and viscosity dependence of boundary locations, especially in under-relaxed situations [15]. The viscosity dependent boundary conditions pose a severe problem for simulating flow through porous media because the permeability becomes viscosity dependent, while it should be a characteristic of the physical properties of porous medium alone. The problem of the viscosity-dependence of the boundary conditions is clearly illustrated by Fig. 1, in which the computed permeability for a typical porous medium GB1b (cf. Section 5) varies significantly as the viscosity changes in the LBGK model. The deficiencies inherent in the LBGK model can be significantly reduced by using a multiple-relaxation-time (MRT) approach [16–22], which separates the relaxation times for different kinetic modes and allows tuning to improve numerical stability and accuracy.

Second, in the LBE simulations of flow through a porous medium, curved fluid–solid interfaces are usually approximated using a zig-zag approach so that the SBB boundary conditions can be directly applied, which reverse the momentum of fluid particles colliding with a solid boundary by mimicking the particle–solid interaction for no-slip boundary conditions. The SBB boundary conditions are easy to implement; they do, however, introduce errors in boundary locations, especially when the resolution is coarse, and using fine enough uniform discretization of pore geometries to adequately resolve the flow with zig-zag approximation is often ineffective and unrealistic computationally. Recently, several schemes have been advanced to more accurately represent such boundaries using spatial interpolations [12,22,23]. These methods can be incorporated separately into LBE model to further improve accuracy and to speed up convergence. However to the best of our knowledge, no systematic quantitative comparison of the numerical accuracy and convergence rate of these methods has been reported in the literature for complex porous medium systems.

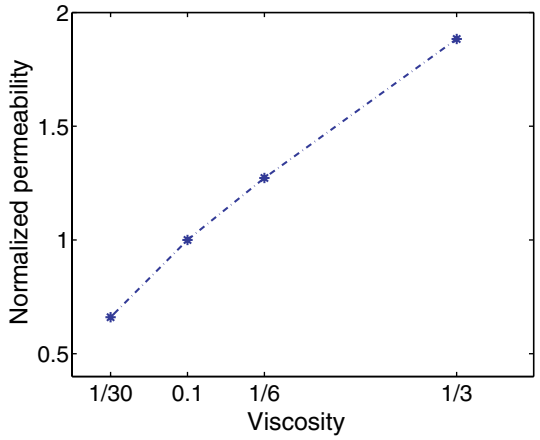

Fig. 1. The viscosity dependence of the computed permeability using the LBGK model. The result is obtained for flow through a sphere-pack medium.

The overall goal of the present work is to examine the accuracy of LBE models for the solution of flow through porous medium systems. The specific objectives of this work are: (1) to implement a standard LBGK and an MRT–LBE model with a number of fluid–solid boundary schemes; (2) to compare the numerical accuracy of available LBE schemes for model problems quantitatively and systematically; and (3) to investigate the discretization level necessary to achieve resolution-independent results for single-phase flow in porous media using various boundary schemes.

The remaining parts of this paper are organized as follows. Section 2 describes briefly the three-dimensional MRT–LBE model with 19 velocities (D3Q19 model) used in this paper. Section 3 discusses the set of fluid–solid boundary conditions to be compared in the work, including the standard bounce-back (SBB) scheme, the linearly interpolated bounce-back (LIBB) scheme, the quadratically interpolated bounce-back (QIBB) scheme, and the multi-reflection (MR) scheme. Sections 4 and 5 present the numerical results for flow through a periodic body-centered cubic (BCC) array of spheres of equal radius and the results for flow through a random-sized sphere-pack porous medium, respectively. Finally, Section 6 concludes the paper.

2. Multiple-relaxation-time LBE model

There are three components in any LBE model. The first component is a discrete phase space consisting of a regular lattice space $\delta_x\mathbb{Z}_d$ with a lattice constant δ_x in d dimensions together with a finite set of highly symmetric discrete velocities $\{\boldsymbol{e}_i | i = 0,1,\ldots,N\}$ connecting each lattice node $\boldsymbol{x}_k \in \delta_x\mathbb{Z}_d$ to its neighbors, and the corresponding set of velocity distribution functions $\{f_i | i = 0,1,\ldots,N\}$ defined on each node of the lattice. The second component is a collision matrix S and $(N+1)$ equilibrium distribution functions $\{f_i^{(\mathrm{eq})} \mid i = 0,1,\ldots,N\}$. The equilibrium distribution functions are functions of the local conserved quantities and are a crucial component of the LBE method, which can be related to kinetic theory. The third component is an evolution equation in discrete time $t_n \in \delta_t\mathbb{N}_0$:

$$\begin{aligned}&\mathbf{f}(\boldsymbol{x}_k + \boldsymbol{e}\delta_t, t_n + \delta_t) - \mathbf{f}(\boldsymbol{x}_k, t_n)\\ &\quad = \mathsf{S}\left[\mathbf{f}^{(\mathrm{eq})}(\boldsymbol{x}_k, t_n) - \mathbf{f}(\boldsymbol{x}_k, t_n)\right] + \mathbf{F},\end{aligned} \tag{1}$$

or equivalently

$$\begin{aligned}&\mathbf{f}(\boldsymbol{x}_k + \boldsymbol{e}\delta_t, t_n + \delta_t) - \mathbf{f}(\boldsymbol{x}_k, t_n)\\ &\quad = \mathsf{M}^{-1}\widehat{\mathsf{S}}[\mathbf{m}^{(\mathrm{eq})}(\boldsymbol{x}_k, t_n) - \mathbf{m}(\boldsymbol{x}_k, t_n)] + \mathbf{F},\end{aligned} \tag{2}$$

where the bold-face symbols, $\mathbf{f}$, $\mathbf{m}$, $\mathbf{m}^{(\mathrm{eq})}$, and $\mathbf{F}$ are B-dimensional (column) vectors ($B = N+1$ or N for models with or without zero velocity, respectively), i.e.,

$$\mathbf{f}(\boldsymbol{x}_k + \boldsymbol{e}\delta_t, t_n + \delta_t) := (f_0(\boldsymbol{x}_k, t_n + \delta_t), \ldots, f_N(\boldsymbol{x}_k + \boldsymbol{e}_N\delta_t, t_n + \delta_t))^{\mathsf{T}},$$
$$\mathbf{f}(\boldsymbol{x}_k, t_n) := (f_0(\boldsymbol{x}_k, t_n), f_1(\boldsymbol{x}_k, t_n), \ldots, f_N(\boldsymbol{x}_k, t_n))^{\mathsf{T}},$$
$$\mathbf{m}(\boldsymbol{x}_k, t_n) := (m_0(\boldsymbol{x}_k, t_n), m_1(\boldsymbol{x}_k, t_n), \ldots, m_N(\boldsymbol{x}_k, t_n))^{\mathsf{T}},$$
$$\mathbf{F} := (F_0, F_1, \ldots, F_N)^{\mathsf{T}}.$$

Here superscript T denotes the transpose operator, and $\mathbf{F}$ represents the external forcing, of which the components are:

$$F_i = 3w_i\rho_0\frac{\boldsymbol{e}_i \cdot \boldsymbol{a}}{c^2}, \tag{3}$$

where $c := \delta_x/\delta_t$, ρ_0 is the (constant) mean density in the system (usually set to 1), $\boldsymbol{a}$ is the acceleration due to external forces, and the weight coefficients for the D3Q19 model are usually chosen as $w_0 = 1/3$, $w_i = 1/18$ for $i = 1$–6, and $w_i = 1/36$ for $i = 7$–18. In lattice units, the time step δ_t is set equal to 1, as is the lattice spacing ($\delta_x = \delta_t = 1$).

The relaxation matrix $\widehat{\mathsf{S}} = \mathsf{M}\cdot\mathsf{S}\cdot\mathsf{M}^{-1}$ is a $B\times B$ diagonal matrix. The transformation matrix M relates the distribution functions represented by $\mathbf{f} \in \mathbb{V} = \mathbb{R}^B$ to their moments represented by $\mathbf{m} \in \mathbb{M} = \mathbb{R}^B$, as in the following:

$$\mathbf{m} = \mathsf{M}\cdot\mathbf{f}, \quad \mathbf{f} = \mathsf{M}^{-1}\cdot\mathbf{m}. \tag{4}$$

The transformation matrix M is constructed from the monomials of the discrete velocity components $e^m_{i\alpha}e^n_{j\beta}\cdots e^l_{k\gamma}$ (α,β and $\gamma \in \{x,y,z\}$) via the Gram–Schmidt orthogonalization procedure [16,19–21]. The row vectors of M are mutually orthogonal, i.e., $\mathsf{M}\cdot\mathsf{M}^{\mathsf{T}}$ is a diagonal matrix, but not normalized so all the matrix elements of M are integers [16,19–21]. For the 19-velocity model in three dimensions, i.e., the D3Q19 model (here DdQq denotes the model with q velocities in d dimensions), the matrix M is given in [20,24].

For the D3Q19 model, the 19 moments are:

$$\mathbf{m} := (\rho, e, \varepsilon, j_x, q_x, j_y, q_y, j_z, q_z, 3p_{xx}, 3\pi_{xx}, p_{ww}, \pi_{ww}, p_{xy}, p_{yz}, p_{xz}, m_x, m_y, m_z)^{\mathsf{T}} = (m_0, m_1, \ldots, m_{18})^{\mathsf{T}},$$

among which, only the density $\rho = \sum_i f_i$ and momentum $\boldsymbol{j} := (j_x, j_y, j_z) = \sum_i f_i\boldsymbol{e}_i$ are conserved quantities for athermal fluids, and the rest are non-conserved quantities [20]. The equilibria $\mathbf{m}^{(\mathrm{eq})}(\rho,\boldsymbol{j})$ for the non-conserved moments are [20]:

$$e^{(\mathrm{eq})} = -11\rho + \frac{19}{\rho_0}\boldsymbol{j}\cdot\boldsymbol{j} = -11\rho + \frac{19}{\rho_0}(j_x^2 + j_y^2 + j_z^2), \tag{5a}$$
$$\varepsilon^{(\mathrm{eq})} = 3\rho - \frac{11}{2\rho_0}\boldsymbol{j}\cdot\boldsymbol{j}, \tag{5b}$$
$$q_x^{(\mathrm{eq})} = -\frac{2}{3}j_x, \quad q_y^{(\mathrm{eq})} = -\frac{2}{3}j_y, \quad q_z^{(\mathrm{eq})} = -\frac{2}{3}j_z, \tag{5c}$$
$$p_{xx}^{(\mathrm{eq})} = \frac{1}{3\rho_0}\left[2j_x^2 - (j_y^2 + j_z^2)\right], \quad p_{ww}^{(\mathrm{eq})} = \frac{1}{\rho_0}\left[j_y^2 - j_z^2\right], \tag{5d}$$
$$p_{xy}^{(\mathrm{eq})} = \frac{1}{\rho_0}j_xj_y, \quad p_{yz}^{(\mathrm{eq})} = \frac{1}{\rho_0}j_yj_z, \quad p_{xz}^{(\mathrm{eq})} = \frac{1}{\rho_0}j_xj_z, \tag{5e}$$
$$\pi_{xx}^{(\mathrm{eq})} = -\frac{1}{2}p_{xx}^{(\mathrm{eq})}, \quad \pi_{ww}^{(\mathrm{eq})} = -\frac{1}{2}p_{ww}^{(\mathrm{eq})},$$
$$m_x^{(\mathrm{eq})} = m_y^{(\mathrm{eq})} = m_z^{(\mathrm{eq})} = 0. \tag{5f}$$

Corresponding the particular order of moments used here, the diagonal relaxation matrix $\widehat{\mathsf{S}}$ is given by

$$\widehat{\mathsf{S}} = \mathrm{diag}(0, s_1, s_2, 0, s_4, 0, s_4, 0, s_4, s_9, s_{10}, s_9, s_{10}, s_{13}, s_{13}, s_{13}, s_{16}, s_{16}, s_{16}) = \mathrm{diag}(0, s_e, s_\varepsilon, 0, s_q, 0, s_q, 0, s_q, s_\nu, s_\pi, s_\nu, s_\pi, s_\nu, s_\nu, s_\nu, s_m, s_m, s_m). \tag{6}$$

The speed of sound of the model is $c_s = 1/\sqrt{3}$ and the viscosity is

$$\nu = \frac{1}{3}\left(\frac{1}{s_\nu} - \frac{1}{2}\right). \tag{7}$$

With the above equilibria of Eqs. (5a), if all of the relaxation rates, $\{s_i | i = 0, \ldots, 18\}$, are set to be a single value $1/\tau$, i.e., $\mathsf{S} = \tau^{-1}\mathsf{I}$, where I is $B\times B$ identity matrix, then the model is equivalent to an LBGK model with the following equilibria [5]:

$$f_i^{(\mathrm{eq})}(\rho, \boldsymbol{u}) = w_i\left[\rho + \rho_0\left(3\boldsymbol{e}_i\cdot\boldsymbol{u} + \frac{9}{2}(\boldsymbol{e}_i\cdot\boldsymbol{u})^2 - \frac{3}{2}\boldsymbol{u}\cdot\boldsymbol{u}\right)\right]. \tag{8}$$

where the fluid velocity $\boldsymbol{u} := \boldsymbol{j}/\rho_0$. When external forcing $\mathbf{F}$ is considered in the LBE simulations, $\boldsymbol{j}' = \boldsymbol{j} + \rho_0\boldsymbol{a}\delta_t/2$ (or $\boldsymbol{u}' = \boldsymbol{u} + \boldsymbol{a}\delta_t/2$), instead of $\boldsymbol{j}$ (or $\boldsymbol{u}$), is used as the measured velocity field for output, and in the calculation of nonlinear velocity terms of the equilibria of Eq. (5a) for the moments (or equilibria of Eq. (8) for the distributions). The reason of replacing $\boldsymbol{j}$ by $\boldsymbol{j}'$ for output and in nonlinear term calculations is to account for the momentum change due to $\mathbf{F}$ and to satisfy the mass conservation equation up to the second-order in the Chapman–Enskog analysis [22,21]. For more detailed discussions of the discrete lattice effects on the external forcing term and MRT–LBE method in general, we refer readers to the literature [16–22].

When simulating flow through porous media, we are often interested in Stokes flow, for which Darcy's law holds. The Stokes flow can be simulated by the *linear* LBE scheme, in which all the nonlinear velocity terms are omitted in the equilibria given by Eq. (5a) for the moments, or equivalently in the the equilibria of Eq. (8) for the distribution functions, i.e.,

$$e^{(\mathrm{eq})} = -11\rho, \quad \varepsilon^{(\mathrm{eq})} = 3\rho, \tag{9a}$$
$$q_x^{(\mathrm{eq})} = -\frac{2}{3}j_x, \quad q_y^{(\mathrm{eq})} = -\frac{2}{3}j_y, \quad q_z^{(\mathrm{eq})} = -\frac{2}{3}j_z, \tag{9b}$$
$$p_{xx}^{(\mathrm{eq})} = p_{ww}^{(\mathrm{eq})} = p_{xy}^{(\mathrm{eq})} = p_{yz}^{(\mathrm{eq})} = p_{xz}^{(\mathrm{eq})} = 0, \tag{9c}$$
$$\pi_{xx}^{(\mathrm{eq})} = \pi_{ww}^{(\mathrm{eq})} = 0, \quad m_x^{(\mathrm{eq})} = m_y^{(\mathrm{eq})} = m_z^{(\mathrm{eq})} = 0. \tag{9d}$$

With the above equilibria, the resulting momentum equation is the Stokes equation without the nonlinear advection term $\boldsymbol{u}\cdot\nabla\boldsymbol{u}$. Note that Darcy's law is only valid for the flow in the limit of zero Reynolds number [25], i.e., the Stokes flow. We will validate the linear LBE scheme in simulations of flow through a simple porous geometry.

3. Solid boundary conditions

The LBE method deals with the single particle distribution function f in phase space $\Gamma := (\boldsymbol{x}, \boldsymbol{\xi})$, as opposed to the hydrodynamic variables, such as fluid density ρ, flow velocity $\boldsymbol{u}$, and temperature T, in physical space $\boldsymbol{x}$. Consequently, the boundary conditions in the LBE method are also expressed in terms of the distribution function f rather than the flow variables commonly controlled in conventional computational fluid dynamics methods. In the LBE method, the objective is to construct the unknown incoming distribution functions based on the known outgoing distribution functions at the boundary nodes so that the physical boundary conditions of interest are satisfied.

The lattice Boltzmann scheme consists of two steps, i.e.,

$$\text{collision}: \quad \tilde{f}_i(\boldsymbol{x}_k, t_n) - f_i(\boldsymbol{x}_k, t_n) = \Omega_i, \tag{10a}$$

$$\text{streaming}: \quad f_i(\boldsymbol{x}_k + \boldsymbol{e}_i\delta_t, t_n + \delta_t) = \tilde{f}_i(\boldsymbol{x}_k, t_n), \tag{10b}$$

where Ω_i denotes the collision operator, and $\tilde{f}_i$ and f_i denote the post- and pre-collision states of the particle distribution functions, respectively. During the streaming step, the no-slip velocity boundary conditions at the fluid–solid interface are usually approximated using the standard bounce-back (SBB) boundary conditions, which mimic the phenomenon that a particle reflects its momentum when colliding with a solid surface.

It is important to stress that the SBB boundary condition does not always place the wall at the one-half grid spacing beyond the last fluid node. In the LBGK model, the actual position of the boundary is viscosity dependent when the SBB is applied. This can be easily seen from the analytic solutions for the Poiseuille flow [15], especially in under-relaxed situations, i.e., when $\tau > 1$. This problem can be solved with the MRT–LBE model when using the linear LBE scheme, by combining the bounce-back rule with a carefully constructed collision operator. Because the boundary location depends on a polynomial of relaxation rates $\{s_i\}$ [17,22], one can choose the relaxation rate s_q for the "energy flux" mode $\boldsymbol{q} := (q_x, q_y, q_z)$ as the following:

$$s_q = 8\frac{(2 - s_v)}{(8 - s_v)}, \tag{11}$$

such that the position where $\boldsymbol{u} = \boldsymbol{0}$ is fixed at exactly one half lattice spacing beyond the last fluid node for Poiseuille flow when the solid walls are parallel to the underlying lattice lines [17,18,22,23].

3.1. Interpolated bounce-back schemes

Fig. 2 illustrates the typical scenario in bounce-back boundary conditions in a one-dimensional setting. If the boundary location $\boldsymbol{x}_W$ is situated half-way between $\boldsymbol{x}_A$ and $\boldsymbol{x}_B$, i.e., $q := |\boldsymbol{x}_A - \boldsymbol{x}_W|/|\boldsymbol{x}_A - \boldsymbol{x}_B| = 1/2$, the incoming distribution function is simply equal to the corresponding outgoing one with the opposite momentum, hence the name "bounce-back" boundary conditions.

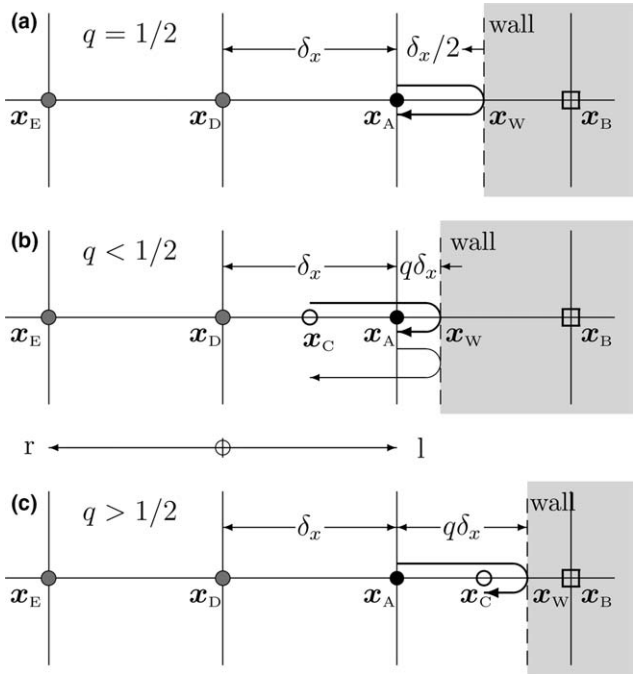

Fig. 2. Illustration of the interpolated boundary conditions in one dimension. Symbols ●, ●, ○ and □ denote interior fluid node, boundary fluid node, the off-lattice location involved in interpolations, and solid node, respectively. (a) the perfect bounce-back situation, $q = 1/2$; (b) interpolation before the bounce-back collision, $q < 1/2$; and (c) interpolation after the bounce-back collision, $q > 1/2$.

Intuitively in the perfect bounce-back situation, in a complete streaming-collision cycle the particle travels half-way between two nodes $\boldsymbol{x}_A$ and $\boldsymbol{x}_B$, collides with the wall at $\boldsymbol{x}_W$, and reverses its momentum (the collision process is assumed not to consume any time), then travels back to $\boldsymbol{x}_A$, as illustrated by Fig. 2(a). When $q < 1/2$, the particle at $\boldsymbol{x}_A$ would end up at $\boldsymbol{x}_C$ after the streaming-collision cycle, as illustrated by the thin arrow in Fig. 2(b). However, if the particle starts from $\boldsymbol{x}_C$, then it will end up at $\boldsymbol{x}_A$ after the streaming-collision cycle, as illustrated by the thick arrow in Fig. 2(b). This can be accomplished if we can construct the distribution function at $\boldsymbol{x}_C$ by using an interpolation *before* the streaming-collision process with the wall takes place. Similarly, when $q > 1/2$, the incoming distribution function can be constructed by using the outgoing one located at $\boldsymbol{x}_C$ *after* the streaming-collision interaction with the wall takes place, as illustrated by the thick arrow in Fig. 2(c), and the distribution function values at nearby nodes $\boldsymbol{x}_D$ and $\boldsymbol{x}_E$.

For stability considerations, we limit ourselves to interpolations, including linear and quadratic interpolations proposed in [23,26]. The linear interpolation bounce-back (LIBB) formulae for $f_L(\boldsymbol{x}_A, t_{n+1}) = \tilde{f}_R(\boldsymbol{x}_C, t_n)$ are:

$$f_{\mathrm{L}}(\boldsymbol{x}_{\mathrm{A}},t_{n+1}) = \begin{cases} (1-2q)\tilde{f}_{\mathrm{R}}(\boldsymbol{x}_{\mathrm{D}},t_n)+2q\tilde{f}_{\mathrm{R}}(\boldsymbol{x}_{\mathrm{A}},t_n), & q<1/2, \\ \left(1-\frac{1}{2q}\right)f_{\mathrm{L}}(\boldsymbol{x}_{\mathrm{D}},t_{n+1})+\frac{1}{2q}f_{\mathrm{L}}(\boldsymbol{x}_{\mathrm{C}},t_{n+1}), & q\geqslant 1/2, \end{cases} \tag{12a}$$

$$= \begin{cases} (1-2q)f_{\mathrm{R}}(\boldsymbol{x}_{\mathrm{A}},t_{n+1})+2q\tilde{f}_{\mathrm{R}}(\boldsymbol{x}_{\mathrm{A}},t_n), & q<1/2, \\ \left(1-\frac{1}{2q}\right)\tilde{f}_{\mathrm{L}}(\boldsymbol{x}_{\mathrm{A}},t_n)+\frac{1}{2q}\tilde{f}_{\mathrm{R}}(\boldsymbol{x}_{\mathrm{A}},t_n), & q\geqslant 1/2. \end{cases} \tag{12b}$$

In the above formulae, subscripts L and R indicate left-bound or right-bound directions, respectively, as depicted in Fig. 2. The interpolation formulae involve either the post-collision information at time t_n or or pre-collision information at time $t_{n+1} := t_n + \delta_t$. Hence, Eq. (12b) indicates that the LIBB requires only local information to perform interpolation. Similarly, the quadratic interpolation bounce-back (QIBB) formulae are:

$$f_{\mathrm{L}}(\boldsymbol{x}_{\mathrm{A}},t_{n+1}) = \begin{cases} q(1+2q)\tilde{f}_{\mathrm{R}}(\boldsymbol{x}_{\mathrm{A}},t_n)+(1-4q^2)\tilde{f}_{\mathrm{R}}(\boldsymbol{x}_{\mathrm{D}},t_n) & \\ \quad -q(1-2q)\tilde{f}_{\mathrm{R}}(\boldsymbol{x}_{\mathrm{E}},t_n), & q<1/2, \\ \frac{2q-1}{q}f_{\mathrm{L}}(\boldsymbol{x}_{\mathrm{D}},t_{n+1})+\frac{1}{q(2q+1)}f_{\mathrm{L}}(\boldsymbol{x}_{\mathrm{C}},t_{n+1}) & \\ \quad +\frac{(1-2q)}{(1+2q)}f_{\mathrm{L}}(\boldsymbol{x}_{\mathrm{E}},t_{n+1}), & q\geqslant 1/2, \end{cases} \tag{13a}$$

$$= \begin{cases} q(1+2q)\tilde{f}_{\mathrm{R}}(\boldsymbol{x}_{\mathrm{A}},t_n)+(1-4q^2)f_{\mathrm{R}}(\boldsymbol{x}_{\mathrm{A}},t_{n+1}) & \\ \quad -q(1-2q)f_{\mathrm{R}}(\boldsymbol{x}_{\mathrm{D}},t_{n+1}), & q<1/2, \\ \frac{2q-1}{q}\tilde{f}_{\mathrm{L}}(\boldsymbol{x}_{\mathrm{A}},t_n)+\frac{1}{q(2q+1)}\tilde{f}_{\mathrm{R}}(\boldsymbol{x}_{\mathrm{A}},t_n) & \\ \quad +\frac{(1-2q)}{(1+2q)}\tilde{f}_{\mathrm{L}}(\boldsymbol{x}_{\mathrm{D}},t_n), & q\geqslant 1/2. \end{cases} \tag{13b}$$

Note that both linear and quadratic interpolations are upwind with respect to the particle velocity ($\boldsymbol{e}_1$ in this case) when $q<1/2$ and downwind when $q>1/2$, and they reduce to the SBB boundary conditions when $q=1/2$.

3.2. Multi-reflection boundary conditions

The multi-reflection (MR) boundary conditions [22] for solving the moving solid boundary problems, on the other hand, utilize a more general closure relation that determines the unknown distributions from five neighboring values. The closure relation is theoretically obtained from the Chapman–Enskog expansion at the boundary nodes. The MR closure relation is accurate up to third-order in the Chapman–Enskog expansion by considering a correction term $E \sim f_i^{(2)}$:

$$f_{\mathrm{L}}(\boldsymbol{x}_{\mathrm{A}},t_{n+1}) = k_1 f_{\mathrm{L}}(\boldsymbol{x}_{\mathrm{C}},t_{n+1})+k_2 f_{\mathrm{R}}(\boldsymbol{x}_{\mathrm{A}},t_{n+1})+k_3 f_{\mathrm{R}}(\boldsymbol{x}_{\mathrm{D}},t_{n+1}) + k_4 f_{\mathrm{L}}(\boldsymbol{x}_{\mathrm{D}},t_{n+1})+k_5 f_{\mathrm{L}}(\boldsymbol{x}_{\mathrm{E}},t_{n+1})+E_L(\boldsymbol{x}_{\mathrm{A}},t_n) \tag{14a}$$

$$= k_1\tilde{f}_{\mathrm{R}}(\boldsymbol{x}_{\mathrm{A}},t_n)+k_2 f_{\mathrm{R}}(\boldsymbol{x}_{\mathrm{A}},t_{n+1})+k_3 f_{\mathrm{R}}(\boldsymbol{x}_{\mathrm{D}},t_{n+1}) + k_4\tilde{f}_{\mathrm{L}}(\boldsymbol{x}_{\mathrm{A}},t_n)+k_5\tilde{f}_{\mathrm{L}}(\boldsymbol{x}_{\mathrm{D}},t_n)+\frac{k_6}{v}f_{\mathrm{L}}^{(2)}(\boldsymbol{x}_{\mathrm{A}},t_n) \tag{14b}$$

where v is the viscosity given by Eq. (7). The coefficients k_i, $i\in\{1,2,\ldots,6\}$ are functions of q and are chosen as follows when the relation between the relaxation parameters of Eq. (11) is used (see detailed formulation in [22]):

$$k_1 = 1, \quad k_2 = -k_4 = \frac{(1-2q-2q^2)}{(1+q)^2}, \quad k_3 = k_5 = \frac{q^2}{(1+q)^2}, \quad k_6 = \frac{1}{4(1+q)^2}. \tag{15}$$

The third-order nonequilibrium terms $f_i^{(2)}$ only relate to the third-order moments (q_x,q_y,q_z) and (m_x,m_y,m_z), and can be explicitly computed as the following:

$$\mathbf{f}^{(2)} = -\mathsf{M}^{-1}\cdot\widehat{\mathsf{S}}\cdot\left[\mathbf{t}-\mathbf{t}^{(\mathrm{eq})}\right], \tag{16a}$$

where $\mathbf{t} := (0,0,0,0,q_x,0,q_y,0,q_z,0,\ldots,0,m_x,m_y,m_z)$. (16b)

The multi-reflection boundary conditions involve five distribution functions at two neighboring nodes of a boundary node, whereas the linear and quadratic interpolations involve two and three distribution functions at one or two neighboring nodes, respectively. The linear and quadratic interpolated boundary conditions are special cases of the multi-reflection boundary conditions with appropriate choices of coefficients $\{k_i\}$ [22].

In cases where there are insufficient fluid nodes to apply the interpolations, we reduce the LIBB to SBB boundary conditions (i.e., $q=1/2$) if there exists only one fluid node between two solid nodes. When only two fluid nodes exist, we reduce the QIBB and MR to LIBB. One can also modify the MR relation of Eq. (14a) by, for example, replacing $f_{\mathrm{R}}(\boldsymbol{x}_{\mathrm{D}},t_{n+1})$ with $f_{\mathrm{R}}(\boldsymbol{x}_{\mathrm{D}},t_n)$, as indicated in [22,27].

Furthermore, regarding parallel implementations, while the LIBB requires only local information, both the QIBB and MR schemes require neighboring information from the boundary nodes. However, the communications are restricted to only the nearest neighbors of the boundary nodes by using the post-collision distributions at time t_n, as demonstrated in Eqs. (13b) and (14b).

A drawback of the interpolation and multi-reflection boundary conditions is that local mass is no longer conserved. However, for incompressible flow with a small density gradient of fluids, a slight violation of the local mass conservation has an insignificant effect on the flow simulations, which will be numerically demonstrated later. It is important to emphasize that an accurate and efficient implementation of the fluid–solid boundary conditions is crucial in porous medium flow simulations with a limited spatial resolution, because applying fine enough discretization of pore geometries to adequately resolve the solid boundaries is often computationally prohibitive. In the following section, we will quantitatively investigate the benefit of the alternative boundary approximations that were discussed above compared to the SBB scheme for porous media simulations.

4. Flow through a body-centered cubic array of spheres

We first considered the case of flow through an idealized porous medium, i.e., a periodic body-centered cubic (BCC) array of spheres of equal radius a, as depicted in Fig. 3. The permeability for this porous medium can be derived analytically [28,29]:

$$\kappa^* = \frac{1}{6\pi a d^*}, \quad d^* = \frac{6\pi a \rho \nu u_{\mathrm{d}}}{F_{\mathrm{D}}}, \tag{17}$$

where u_{d} is the Darcy velocity along the flow direction, and F_{D} is the drag force for each sphere. The inverse of the dimensionless drag, d^*, is purely determined by the geometric characteristics of the sphere array, and can be given by a function of the solid volume fraction c as a series expansion:

$$d^* = \sum_{n=0}^{30} \alpha_n \chi^n, \quad \chi = \left(\frac{c}{c_{\max}}\right)^{1/3},$$
$$c = \frac{8\pi a^3}{3L^3}, \quad c_{\max} = \frac{\sqrt{3}\pi}{8}, \tag{18}$$

where L is the length of the cube, as shown in Fig. 3(b), and the coefficients α_n are given in [29]. Various resolutions N^3 are used in our simulations. Obviously, in lattice units, the sphere radius is $\zeta = \sqrt{3}N\chi/4$, and the pore throat (i.e., the minimum space between solid spheres) is $\eta = \sqrt{3}N(1-\chi)/2$.

We measure the fluid permeability κ according to Darcy's law:

$$u_{\mathrm{d}} = -\frac{\kappa}{\rho\nu}(\nabla_z p + \rho g), \tag{19}$$

where the Darcy velocity u_{d} is obtained as the volume averaged fluid velocity (u_z') over the system [30], ρg is the strength of the forcing, and z is the vertical coordinate parallel to the forcing direction.

For the D3Q19 model, in addition to the relaxation rate s_ν, which determines the viscosity ν, there are five other relaxation rates that are adjustable parameters: s_e, s_ε, s_q, s_π, and s_m. To evaluate the effect of the adjustable relaxation parameters s_i of the MRT scheme to the flow simulations, two sets of relaxation parameters are studied here:

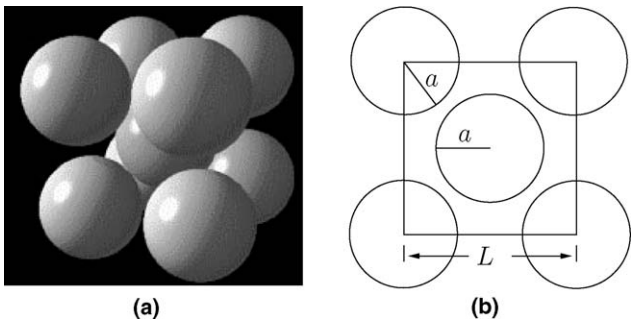

Fig. 3. A BCC array of spheres with equal radii. (a) 3D view (black and gray area depict fluid and solid regions, respectively); and (b) a 2D projection.

$$\text{Set A}: s_\nu = \frac{1}{\tau} = \frac{2}{(6\nu+1)}, \quad s_e = s_\varepsilon = s_\pi = s_m = s_q = 8\frac{(2-s_\nu)}{(8-s_\nu)}, \tag{20}$$

$$\text{Set B}: s_e = s_\varepsilon = s_\pi = s_\nu = \frac{1}{\tau}, \quad s_m = s_q = 8\frac{(2-s_\nu)}{(8-s_\nu)}. \tag{21}$$

Set A of Eq. (20) follows our previous work based on empirical observations [31], and Set B of Eq. (21) follows the two-relaxation-time (TRT) model proposed in [22,32,33] based on the Chapman–Enskog analysis, in which the even-order modes are relaxed with the relaxation rate s_ν determined by the viscosity, while the odd-order ones with the relaxation rate s_q given by Eq. (11) so that the actual locations of walls are viscosity independent when the standard bounce-back boundary conditions are used.

In this section, we tested the validity of the *linear* lattice Boltzmann equation as we compared the LBE simulations to the analytical solution of Stokes flow through the BCC array of spheres. Hereafter, the linear LBE was used unless otherwise stated, and acronyms MRT–MR, MRT–QIBB, MRT–LIBB, MRT–SBB are used to denote the MRT scheme with multi-reflection, quadratic interpolations, linear interpolations, and the standard bounce-back boundary conditions, respectively, and BGK–SBB denotes the LBGK scheme with the standard bounce-back boundary conditions.

4.1. Viscosity effect on permeability

We first evaluated the viscosity dependence of the computed permeability by using different LBE schemes. Fig. 4(a) and (b) show the normalized permeability κ/κ^* for the BCC array of spheres with $\chi = 0.85$, where κ^* is given by Eq. (17), at $\tau = 1/s_\nu = 0.6$, 0.8, 1.0, 1.5, and 2.0 and with, respectively, the relaxation parameters of Set A and Set B. The resolution used was 32^3, corresponding to the sphere radius $\zeta \approx 11.8$ and the pore throat $\eta \approx 2.8$ in lattice units, which are sufficient to apply LIBB, QIBB, and MR schemes. The results clearly show that the values of κ/κ^* obtained by the MRT–SBB scheme are much less dependent on viscosity than those obtained by the BGK–SBB scheme, and when using the relaxation rates of Set B, κ is independent of ν. In all cases, the results obtained with the MRT–SBB scheme are consistently better than those obtained with the BGK–SBB.

For the MRT–LBE with different boundary conditions, we observed the following. First, it is clear that, as shown in Fig. 4, the MR boundary conditions significantly improve the results of κ when compared to QIBB, LIBB, and SBB boundary conditions, and yield virtually viscosity-independent results with either set of relaxation values. Second, with a fixed viscosity, the permeability monotonically increases when using the SBB, LIBB, and QIBB boundary conditions. The SBB consistently under-predicts the permeability because its inaccuracy in geometry representation, whereas the LIBB and QIBB boundary

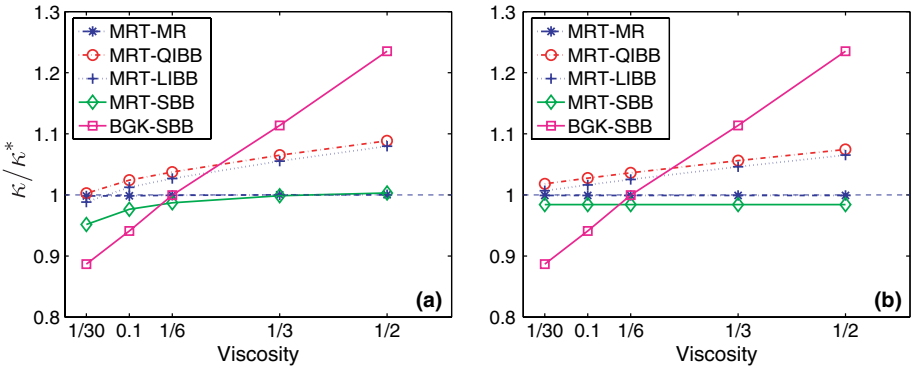

Fig. 4. The normalized permeability κ/κ^* for the BCC array of spheres vs. the viscosity v. The porosity is $\chi = 0.85$ and the resolution is 32^3. The relaxation rates used are: (a) Set A given by Eq. (20) and (b) Set B given by Eq. (21).

conditions also over-predict in most cases, and more so the QIBB than the LIBB. Third, the LIBB and QIBB boundary conditions seem to work better than the SBB only in the over-relaxed cases ($\tau = 1/s_v < 1$), which require more iterations to reach the steady state than for the under-relaxed cases ($\tau > 1$). Later this point will be further studied quantitatively. And fourth, unlike the *nonlinear* LBE simulations for the Navier–Stokes flows, in which the QIBB leads to more accurate velocity fields than the LIBB [23], we found that, with the *linear* LBE, the QIBB does not seem to significantly improve the accuracy compared to the LIBB counterpart, although the QIBB boundary conditions appear to be more accurate for over-relaxed cases (e.g., $\tau = 0.6$). One reason for this is because the resolution used in this test is sufficiently refined so that the computed permeabilities are relatively insensitive to the boundary conditions. This issue will be further addressed in the following section.

4.2. Sphere size effect

To quantify the discretization error related to the boundary conditions, we performed MRT–LBE simulations for the periodic BCC arrays of spheres by varying the sphere radius (porosity ϕ between 0.42 and 0.92) at the fixed resolution 32^3. With decreasing porosity ϕ at a fixed resolutions N^3, the pore throat η shrinks, effectively reducing the resolution of the pore structure. Table 1 shows the relative error $\delta\kappa = (\kappa/\kappa^* - 1)$ for the normalized permeability κ/κ^*, and the number of iteration T required to reach a steady state, using MRT–MR, MRT–QIBB, MRT–LIBB, and MRT–SBB schemes. For the MR scheme, we compared two cases, $\tau = 2.0$ and $\tau = 0.6$, while only $\tau = 0.6$ was applied to the QIBB, LIBB, and SBB boundary conditions. We also compared the permeabilities obtained by the linear LBE to those obtained by the nonlinear LBE for a medium with the least resolved pore space, i.e., the medium with $\chi = 0.95$. The force magnitude was set to be $g = 10^{-4}$ and 10^{-5} for the nonlinear LBE simulations, corresponding to Reynolds number $Re = 1.9$ and 0.19, respectively.

Based on the results in Table 1, we made the following observations:

- When over-relaxed, all of the interpolated schemes lead to significant improvement in the estimation of κ when compared to the SBB boundary conditions for a wide range of χ.
- When comparing the QIBB and LIBB schemes, the errors in κ obtained by the QIBB are considerably smaller than those by the LIBB, particularly when χ approaches 1, the cases in which the pore spaces are insufficiently resolved, as indicated by small pore throat η.
- The MR boundary condition in general leads to significantly more accurate permeability predictions than any other schemes.
- When pore space is sufficiently resolved, the MR scheme with $\tau > 1$ is recommended because it yields accurate results with relatively few iterations. However, the MR scheme is prone to numerical instability when $\tau = 1/s_v < 0.8$ because the term $E \sim f^{(2)}/v$ in Eq. (14a) may become too large with a small v.
- For a single-phase simulation of a BCC array of spheres at resolution level $\zeta = 13.2$ and $\eta = 1.4$, the difference between the linear and nonlinear LBE permeabilities is within 0.3% at $Re \approx 2$, and within 0.001% at $Re \approx 0.2$.

4.3. Discretization effect

We next investigated the discretization effect for Stokes flow through a BCC array of spheres. We fixed the porosity at $\chi = 0.85$ and varied the resolution N^3, for $N = 8$, 16, 24, 32, 48, 64, and 96, which correspond to a sphere radius $\zeta = 2.9$, 5.8, 8.8, 11.8, 17.6, 23.6, and 35.3 lattice spacings. We show the normalized permeability obtained with a discretization N, κ_N/κ^*, using the relaxation parameters in Set A and Set B in Fig. 5(a) and (b), respectively. The results confirm that interpolation improves the accuracy of the SBB boundary conditions.

Table 1
The relative errors of the permeability $\delta\kappa$ (%) and number of iteration time steps T for a set of periodic BCC arrays of spheres with varying χ using various schemes

χ	ϕ	η	s_i	MRT–MR $\tau = 2.0$		MRT–MR $\tau = 0.6$		MRT–QIBB $\tau = 0.6$		MRT–LIBB $\tau = 0.6$		MRT–SBB $\tau = 0.6$	
				$\delta\kappa$(%)	$\frac{T}{100}$	$\delta\kappa$(%)	$\frac{T}{100}$	$\delta\kappa$(%)	$\frac{T}{100}$	$\delta\kappa$(%)	$\frac{T}{100}$	$\delta\kappa$(%)	$\frac{T}{100}$
0.5	0.92	13.8	A	0.01	12	−0.35	159	0.58	148	0.09	125	−2.18	123
			B	−0.13	12	−0.13	148	1.24	148	0.76	149	−0.68	148
0.6	0.85	11.1	A	0.08	9	−0.02	36	0.84	84	−0.24	83	−5.21	80
			B	0.02	9	0.02	98	1.45	98	0.58	95	−3.65	95
0.7	0.76	8.3	A	0.02	6	−0.45	54	0.43	54	−0.83	54	−6.05	52
			B	−0.11	6	−0.11	63	1.29	63	0.26	63	−3.98	62
0.8	0.64	5.5	A	0.20	4	−0.02	40	0.60	40	−1.62	39	−9.38	36
			B	0.09	4	0.09	40	1.79	40	0.11	39	−8.31	37
0.85	0.59	4.2	A	0.03	3	−0.16	36	0.27	30	−1.17	30	−4.84	30
			B	−0.08	11	−0.08	30	1.82	30	0.69	30	−1.58	30
0.9	0.50	2.8	A	0.34	2	*0.02	*8	0.72	25	−1.66	23	−8.21	22
			B	0.24	2	0.04	23	2.61	23	0.51	23	−4.34	22
0.95	0.42	1.4	A	1.63	2	−2.06	18	−0.55	17	−3.07	17	−10.1	16
			B	0.83	2	0.02	17	2.35	17	0.23	17	−5.27	16
†0.95	$Re = 1.9$		A	1.63	2	−2.32	15	0.81	17	−3.32	17	−10.3	16
†0.95	$Re = 0.19$		A	1.63	2	−2.06	17	0.55	17	−3.07	17	−10.1	16

ϕ is the porosity and η is the lattice size of pore throat. The grid resolution is 32^3 and the forcing magnitude $g = 10^{-4}$. The relaxation parameters s_i in Set A and Set B are used in the comparison. Values with $*$ were obtained at $\tau = 0.8$ as MR boundary conditions could become numerically unstable at $\tau < 0.8$. To test the validity of the linear LBE, the last two lines with Re show the results using the nonlinear LBE terms for a medium with $\chi = 0.95$.

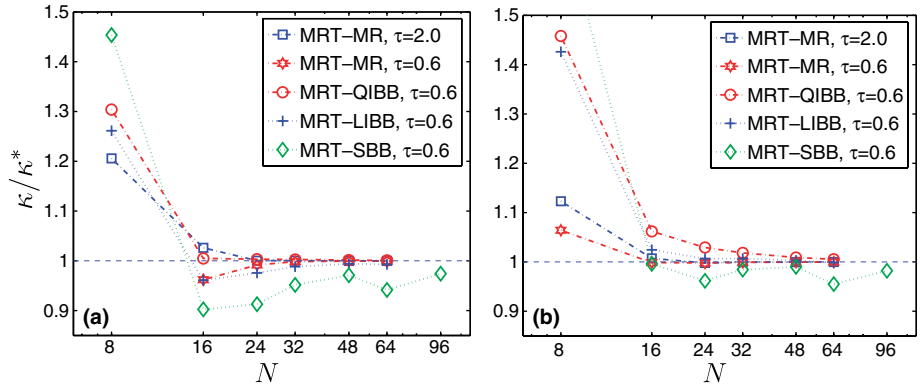

Fig. 5. The normalized permeability κ/κ^* as a function of grid resolution N in each dimension for the BCC array of spheres with $\chi = 0.85$. The relaxation parameters used are: (a) Set A given by Eq. (20) and (b) Set B given by Eq. (21).

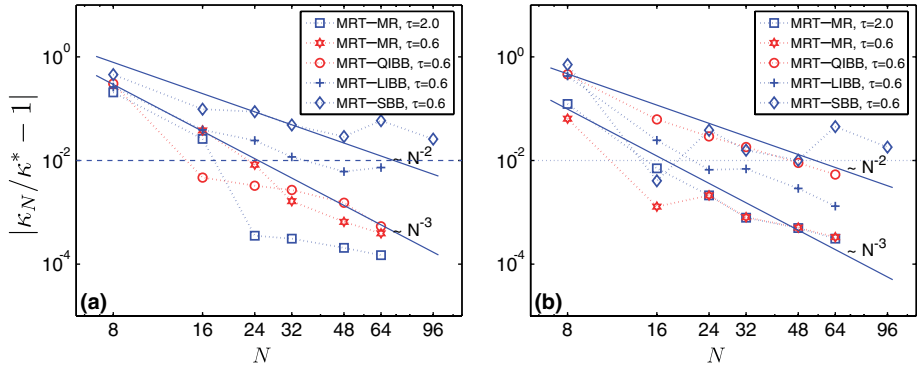

Fig. 6. Relative error of permeability $|k_N/k^* - 1|$ as a function of grid resolution N in each dimension for the BCC array of spheres with $\chi = 0.85$, using relaxation parameters of (a) Set A and (b) Set B.

To clearly show the discretization effects, Fig. 6(a) and (b) illustrate, respectively, the absolute relative error $|\delta\kappa_N| = |\kappa_N/\kappa^* - 1|$ of κ_N as a function of grid resolution N for the relaxation parameters of the Set A and Set B. We consider κ_N is discretization independent if $|\delta\kappa_M| < 1\%$ for any $M \geqslant N$. Hence, Fig. 6(a) indicates that for the BCC array of spheres, with relaxation parameters of Set A, κ_N becomes grid independent if $N \geqslant 16$ when using the QIBB boundary conditions, $N \geqslant 24$ when using MR, and $N \geqslant 48$ when using LIBB, while with the SBB boundary conditions, κ likely converges to a constant value at a discretization level $N \gg 96$. Fig. 6(b), on the other hand, indicates that with the relaxation parameters given by Set B, κ becomes discretization independent if $N \geqslant 16$ for MR, $N \geqslant 24$ for LIBB, and $N \geqslant 48$ for QIBB.

These results indicate that the choice of the relaxation parameters has a significant effect on the permeability computed with different boundary conditions. The effects on the QIBB and LIBB boundary conditions appear to be more severe than those on the MR and SBB boundary conditions. For example, with the relaxation parameters of Set A, the MRT–QIBB scheme converges to the analytic solution at a mesh size that is $1/3^3$ of what required with that of Set B. And, with relaxation parameters of Set B, the MRT–LIBB scheme appears to perform better compared to the MRT–QIBB scheme.

It is clear that the computed permeability shown in Fig. 6 has not reached the asymptotic limit in which the order of convergence can be demonstrated using Richardson's formula. However, the results based on linear regression of the data shown in Fig. 6 clearly indicate that the MRT–LBE with all the boundary conditions, i.e., the MR, QIBB, LIBB, and SBB, has a second-order or better rate of convergence, depending on the boundary conditions and the choice of the relaxation parameters.

4.4. Computational issues

In terms of computational time, we find that the MRT model generally takes about $10 \sim 20\%$ more CPU time than the LBGK model due to additional computation in moment space. It is noteworthy that no more computational time than the LBGK model is needed when using the the two-relaxation-time (TRT) model with the form of the TRT link collision operator [32,33], which uses a collision operator with two relaxation rates for even and odd-order moments so that no projection to the moment space is needed.

Regarding the computational efficiency of the different boundary schemes, we found that these schemes require no more run time compared to the SBB method when using a moderate number of processors (with a fixed resolution of 64^3 and up to 32 processors). Even though additional communication is required for both the MR and QIBB schemes, we have observed in our previous study [34] that LBE methods are dominated by the computations required and the total communication time contributes a small part of the total execution time. Additionally, using asynchronous communication to overlap the processing of message transfers and computations further limits the effect of communication on total run time. The only disadvantage associated with the interpolation schemes is the overhead due to the calculation of boundary locations, i.e., the array for q at boundary nodes. However, the array for q values only needs to be computed once at the pre-processing for each LBE simulation with different medium or resolution.

5. Flow through a random-sized sphere pack medium

In this section, we present results for LBE simulations of flow through a more complex porous medium, which is intended to mimic an experimental medium GB1b [35]. The experimental medium GB1b was represented using a random sphere pack generated in [36] using the algorithm developed in [37]. The simulated porous media can be readily generated using this approach with specified porosity ϕ and the probability density function of the grain size distribution, measured from real porous media. This approach has yielded good agreement between simulated sphere packs and real porous media in terms of flow measurements [30,37,38].

The porosity of the GB1b medium simulate was 0.36; the mean grain diameter was 0.1149 (mm) and the relative standard deviation of the grain size was 4.7%. To achieve reliable packings, the entire sphere pack included about 10,000 spheres in a cube of size 13 (mm^3). For the case of comparison of different boundary conditions, we used a small subset of the entire GB1b sphere-pack in this work, which contained about 23 spheres. The geometry of the medium is shown in Fig. 7. The sphere-pack algorithm generated the center locations and radii of the spheres, which were used to determine the exact boundary locations with respect to the lattice, i.e., the parameter q, the fraction in fluid region of a grid spacing intersected by a boundary. For flow simulations through the sphere pack GB1b, the

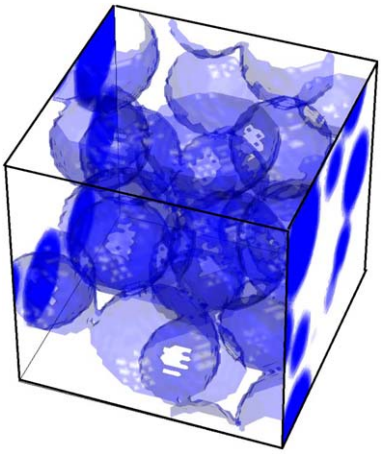

Fig. 7. A subset of the GB1b pore geometry used in the simulations. Colored and transparent areas are for solid and fluid spaces, respectively.

nonlinear LBE was used to solve for the Navier–Stokes equation. We kept the volume averaged Reynolds number $Re < 0.1$ for each simulation, but higher local Reynolds numbers were expected due to the complex pore geometry.

5.1. Viscosity effect

Similar to Fig. 4, we show in Fig. 8(a) and (b) the viscosity dependence of the permeability obtained by all the schemes, with a resolution of 64^3, corresponding to an averaged grain radius $\zeta = 11.2$. This resolution is comparable to the resolution 32^3 for the BCC array of spheres with $\chi = 0.85$, as shown in Fig. 4 of Section 4.1, in which $\zeta = 11.8$. Hence, we can directly compare the viscosity dependence of the permeabilities in different porous media. Because of the exact solution of κ for the medium domain is unknown, a computed permeability with a fine resolution of 200^3 and the MRT–MR scheme using relaxation parameter Set B was considered indicative of the true permeability of the medium, which was used as κ_{ref} unless otherwise stated.

As shown in Figs. 4 and 8, for all the schemes tested here, the viscosity-dependence of the permeability is similar in the BCC array of spheres and the GB1b sphere-pack. While the MRT–SBB and MRT–MR results of κ remain virtually viscosity-independent with Set B, small dependence κ on viscosity is observed using MRT–SBB and MRT–MR with Set A. For the MRT–QIBB, MRT–LIBB, and BGK–SBB schemes, the viscosity-dependence of κ for the GB1b porous medium is somewhat larger than that for the BCC array of spheres, as expected, because of the more complex solid boundaries in the GB1b porous medium than those in the BCC array of spheres.

5.2. Discretization effect

We next evaluated the discretization effect for the GB1b porous medium. The resolutions used to compute the κ were 8^3, 16^3, 24^3, 32^3, 48^3, and 64^3, corresponding to $\zeta = 1.4$, 2.8, 4.2, 5.6, 8.4, and 11.2, respectively. Fig. 9(a) and (b) show the κ_N/k_{ref} vs. N using the MRT–MR, MRT–QIBB, MRT–LIBB, and MRT–SBB schemes at $\tau = 0.6$ with the relaxation parameters of Set A and Set B, respectively. Correspondingly, Fig. 10(a) and (b) show the relative error $|\delta\kappa| = |\kappa_N/\kappa_{\text{ref}} - 1|$ vs. N.

Again, we considered that the computed κ reaches its resolution-independent value at a resolution N^3 if $|\delta\kappa_M| < 1\%$ for any $M \geqslant N$. Since the SBB scheme does not converge to κ_{ref} obtained by the MRT–MR scheme, as shown in Fig. 9, the relative errors of permeability obtained by the SBB were plotted in Fig. 10 with respect to κ_{200} using the respective scheme, rather than

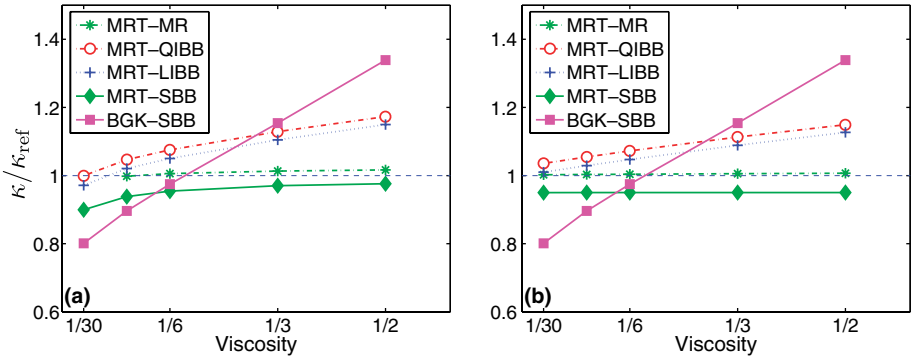

Fig. 8. The normalized permeability $\kappa/\kappa_{\text{ref}}$ vs. the viscosity ν for a portion of the GB1b sphere-pack porous medium. The resolution is 64^3. The relaxation parameters used in the MRT–LBE models are: (a) Set A and (b) Set B.

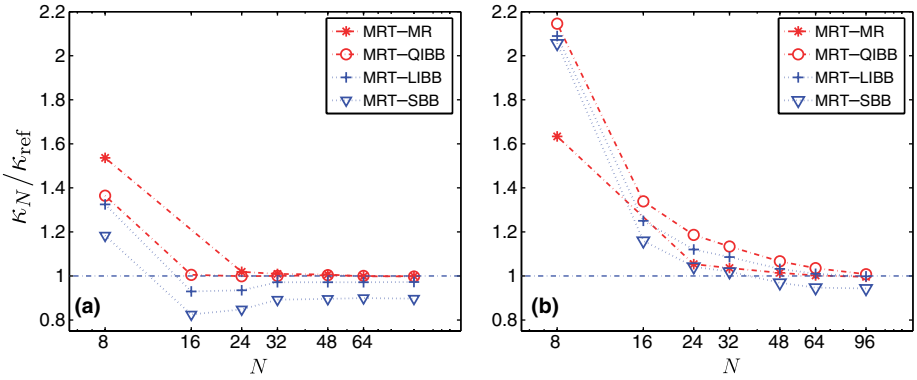

Fig. 9. The normalized permeability $\kappa/\kappa_{\text{ref}}$ as a function of grid resolution N in each dimension. The relaxation parameters used in the MRT–LBE models are: (a) Set A and (b) Set B.

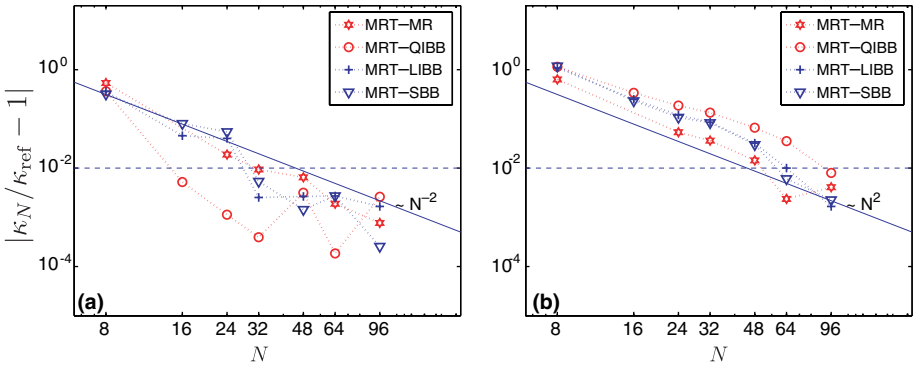

Fig. 10. The relative error of permeability $|k_N/k_{\rm ref}-1|$ as a function of grid resolution N in each dimension. The relaxation parameters used in the MRT schemes are: (a) Set A and (b) Set B. Since the SBB and LIBB do not converge to $\kappa_{\rm ref}$ obtained by MRT–MR scheme, the errors by the MRT–SBB and MRT–LIBB were compared with respect to $\kappa_{\rm ref}$ obtained by respective schemes in order to show clearly the order of convergence.

MRT–MR. We observed that the SBB boundary condition with relaxation parameter Set A yields a discretization-independent κ for the GB1b medium at $N \geqslant 32$, i.e., $\zeta \geqslant 5.6$. This is in good agreement with our previous study [30], showing that for homogeneous and heterogeneous sphere packings, κ becomes discretization independent if $\zeta \geqslant 6$ with the SBB boundary condition. It is noteworthy that when using the SBB scheme significantly smaller discretization level is needed to yield discretization-independent κ for the sphere-pack medium, compared to the BCC array of spheres, as depicted in the earlier section.

When interpolated boundary conditions are applied, discretization-independent κ can be achieved at a coarser resolution level, i.e., at $\zeta \geqslant 2.8$ when using the QIBB boundary condition with Set A. However, for MR and LIBB with Set A, this condition becomes $\zeta \geqslant 5.6$. Once again, we observed that the convergence behavior of κ strongly depends on the relaxation parameters. At coarser resolutions, the permeability values obtained with Set B parameters are noticeably higher than the corresponding values obtained with Set A parameters. For the MRT–SBB and MRT–LIBB schemes, κ converges to a constant value when $\zeta \geqslant 11.2$, whereas for MRT–MR and MRT–QIBB schemes, κ converges to a constant value when $\zeta \geqslant 16.8$. Although second-order convergence is observed from the results obtained from all schemes with different sets of parameters and the two-relaxation-time parameters of Set B lead to a more consistent convergent behavior, Set A seems to be more advantageous because it leads to more accurate flow simulations at coarser discretization level.

6. Discussion and summary

In this work, we observe that the MRT models significantly reduce the viscosity dependence of permeability in LBE porous medium simulations. The reason is that in the MRT models, the location where the exact flow boundary conditions are satisfied can be essentially viscosity independent by specifying an appropriately constructed collision operator, while it is impossible to achieve this result for an LBGK model. Our results for flow through both a BCC array of spheres and a random-sized sphere-pack clearly demonstrate the advantage of the MRT models over the LBGK models.

To improve numerical accuracy of the geometric representation for arbitrary boundaries, we investigated several boundary schemes, including linear interpolation bounce-back (LIBB), quadratic interpolation bounce-back (QIBB), and multi-reflection (MR) schemes. From flow simulations for a BCC array of spheres, we showed that all of the interpolation schemes can significantly improve the accuracy of simulations when compared to the SBB approaches, provided that resolution is sufficient to apply the interpolations. In general, the MR scheme yielded the most accurate and virtually viscosity-independent permeability results, while the improvement due to the LIBB and QIBB was significant in over-relaxation cases ($\tau < 1$). In addition, the MR scheme with $\tau > 1$ significantly reduced the iterations required to reach a steady state. However, the MR scheme with $\tau < 0.8$ may be prone to numerical instability and this issue needs to be further investigated.

We also noticed that the permeability monotonically increased from the value obtained using the SBB scheme to that of the MR, LIBB, and QIBB schemes. The SBB scheme tended to under-predict the permeability, whereas the LIBB and QIBB over-predicted the permeability. It is important to note that in the linear LBE simulations, the quadratic interpolations do not lead to more accurate results than the linear interpolations, as one would expect in the Navier–Stokes simulations [23]. We believe that this is due to a significant nonequilibrium effect, which is explicitly dealt with only in the MR boundary conditions.

The results for the flow through the BCC array of spheres showed that with the relaxation parameter Set A, the QIBB and MR schemes converged to the analytical solution of permeability at a mesh size that is at least $1/4^3$ of what is required for SBB scheme to achieve discretization-independent permeability. For flow through a sphere-pack porous medium, with Set A parameters, the QIBB scheme converged at $1/2^3$ of the mesh size required by the corresponding SBB scheme. The observation that the interpolated boundary schemes yielded more accurate

flow simulation at coarser discretization and with shorter iteration time is crucial in porous medium flow simulations, because computational limitations are commonplace for standard problems of concern.

We further find that the choice of the relaxation parameters has a significant effect on the flow simulations using different schemes. In particular, the effect of the linear and quadratic interpolations on the permeability has a stronger dependence on the relaxation parameters than the SBB and MR counterparts. The two-relaxation-time parameters (Set B) can yield exact viscosity-independent permeability with the SBB and MR boundary conditions. However, Set A can also be advantageous because it allows the QIBB and MR schemes to converge to an accurate solution even at coarser resolutions.

Acknowledgement

The authors are grateful to Dr. I. Ginzburg for insightful discussions. This work was supported in part by National Science Foundation (NSF) grant DMS-0327896 and grant P42 ES05948 from the National Institute of Environmental Health Sciences.

References

[1] McNamara GR, Zanetti G. Use of the Boltzmann equation to simulate lattice-gas automata. Phys Rev Lett 1988;61(20):2332–5.
[2] Higuera FJ, Jiménez J. Boltzmann approach to lattice gas simulations. Europhys Lett 1989;9:663–8.
[3] Frisch U, Hasslacher B, Pomeau Y. Lattice-gas automata for the Navier–Stokes equation. Phys Rev Lett 1986;56:1505–7.
[4] Frisch U, d'Humières D, Hasslacher B, Lallemand P, Pomeau Y, Rivet J-P. Lattice gas hydrodynamics in two and three dimensions. Complex Syst 1987;1:649–707.
[5] He X, Luo L-S. A priori derivation of the lattice Boltzmann equation. Phys Rev E 1997;55:R6333–6.
[6] He X, Luo L-S. Theory of lattice Boltzmann method: from the Boltzmann equation to the lattice Boltzmann equation. Phys Rev E 1997;56:6811–7.
[7] Junk M, Klar A. Discretizations for the incompressible Navier–Stokes equations based on the lattice Boltzmann method. SIAM J Sci Comput 2000;22:1–19.
[8] Junk M. A finite difference interpretation of the lattice Boltzmann method. Numer Methods Part Diff Equat 2001;17:383–402.
[9] Junk M, Yong W-A. Rigorous Navier–Stokes limit of the lattice Boltzmann equation. Asymptotic Anal 2003;35:165–85.
[10] Junk M, Klar A, Luo L-S. Asymptotic analysis of the lattice Boltzmann equation. J Computat Phys 2005;210(2):676–704.
[11] Chen S, Doolen GD. Lattice Boltzmann method for fluid flows. Annu Rev Fluid Mech 1998;30:329–64.
[12] Yu D, Mei R, Luo L-S, Shyy W. Viscous flow computations with the method of lattice Boltzmann equation. Prog Aerosp Sci 2003;39:329–67.
[13] Chen H, Chen S, Matthaeus WH. Recovery of the Navier–Stokes equations using a lattice-gas Boltzmann methods. Phys Rev A 1992;45:5339–42.
[14] Qian YH, d'Humières D, Lallemand P. Lattice BGK models for Navier–Stokes equation. Europhys Lett 1992;17(6):479–84.
[15] He X, Zou Q, Luo L-S, Dembo M. Analytic solutions and analysis on non-slip boundary condition for the lattice Boltzmann BGK model. J Stat Phys 1997;87:115–36.
[16] d'Humières D. Generalized lattice-Boltzmann equations. In: Shizgal BD, Weave DP, editors. Rarefied gas dynamics: theory and simulations, volume 159 of Prog Astronaut Aeronaut, Washington (DC), 1992. AIAA, p. 450–8.
[17] Ginzbourg I, Adler PM. Boundary flow condition analysis for the three-dimensional lattice Boltzmann model. J Phys II 1994;4:191–214.
[18] Ginzburg I, d'Humières D. Local second-order boundary methods for lattice Boltzmann models. J Stat Phys 1996;84(5/6):927–71.
[19] Lallemand P, Luo L-S. Theory of the lattice Boltzmann method: dispersion, dissipation, isotropy, Galilean invariance, and stability. Phys Rev E 2000;61(6):6546–62.
[20] d'Humières D, Ginzburg I, Krafczyk M, Lallemand P, Luo L-S. Multiple-relaxation-time lattice Boltzmann models in three dimensions. Philos Tran Roy Soc Lond A 2002;360:437–51.
[21] Lallemand P, Luo L-S. Theory of the lattice Boltzmann method: acoustic and thermal properties in two and three dimensions. Phys Rev E 2003;68:036706.
[22] Ginzburg I, d'Humières D. Multireflection boundary conditions for lattice Boltzmann models. Phys Rev E 2003;68:066614.
[23] Bouzidi M, Firdaouss M, Lallemand P. Momentum transfer of a Boltzmann-lattice fluid with boundaries. Phys Fluids 2001;13(11):3452–9.
[24] Yu H, Luo L-S, Girimaji SS. LES of turbulent square jet flow using an MRT lattice Boltzmann model. Comput Fluids, this issue, doi:10.1016/j.compfluid.2005.04.009.
[25] Firdaouss M, Guermond JP, Le Quéré P. Nonlinear correction to Darcy's law at low Reynolds numbers. J Fluid Mech 1997;343:331–50.
[26] Lallemand P, Luo L-S. Lattice Boltzmann method for moving boundaries. J Computat Phys 2003;184:406–21.
[27] Ginzburg I. Generic boundary conditions for lattice Boltzmann models and their application to advection and anisotropic-dispersion equations. Adv Water Res 2005;28:1196–216.
[28] Hasimoto H. On the periodic fundamental solutions of the Stokes equation and their application to viscous flow past a cubic array of spheres. J Fluid Mech 1959;5:317–28.
[29] Sangani AS, Acrivos A. Slow flow through a periodic array of spheres. Int J Multiphase Flow 1982;8(4):343–60.
[30] Pan C, Hilpert M, Miller CT. Pore-scale modeling of saturated permeabilities in random sphere packings. Phys Rev E 2001;64(6):066702.
[31] Pan C, Luo L-S, Miller CT. An evaluation of lattice Boltzmann equation methods for simulating flow through porous media. In: Proceedings of the XVth International Conference on Computational Methods in Water Resources, Chapel Hill, 2004. Elsevier, p. 95–106.
[32] Ginzburg I, Carlier J-P, Kao C. Lattice Boltzmann approach to Richards' equation. In: Proceedings of the XVth International Conference on Computational Methods in Water Resources, Chapel Hill, 2004. Elsevier, p. 15–23.
[33] Ginzburg I. Variably saturated flow described with the anisotropic lattice Boltzmann methods. Comput Fluids, this issue, doi:10.1016/j.compfluid.2005.11.001.
[34] Pan C, Prins JF, Miller CT. A high-performance lattice Boltzmann implementation to model flow in porous media. Comput Phys Commun 2004;158(2):89–105.
[35] Hilpert M, McBride JF, Miller CT. Investigation of the residual-funicular nonwetting-phase-saturation relation. Adv Water Res 2001;24(2):157–77.
[36] Hilpert M, Miller CT. Pore-morphology-based simulation of drainage in totally wetting porous media. Adv Water Res 2001;24(3/4):243–55.
[37] Yang A, Miller CT, Turcoliver LD. Simulation of correlated and uncorrelated packing of random size spheres. Phys Rev E 1996;53(2):1516–24.
[38] Pan C, Hilpert M, Miller CT. Lattice-Boltzmann simulation of two-phase flow in porous media. Water Resour Res 2004;40(1):W01501:1–W01501:14.